

Fabricating Spatially-Varying Subsurface Scattering

Yue Dong^{*†} Jiaping Wang[†] Fabio Pellacini[‡] Xin Tong[†] Baining Guo^{*†}
^{*}Tsinghua University [†]Microsoft Research Asia [‡]Dartmouth College

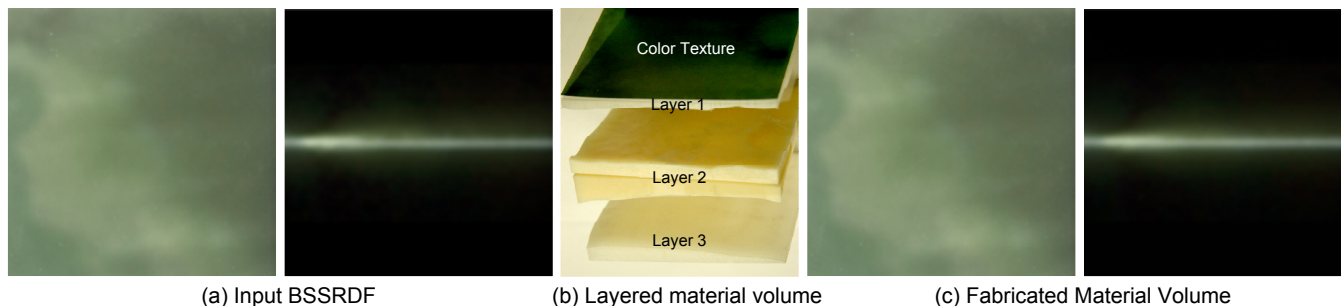


Figure 1: Our system automatically generates a layered material volume for approximating a custom BSSRDF. (a) The appearance of a real material sample under diffuse lighting and a beam light. (b) A collection of layers generated by our system for assembling the output volume. (c) The appearance of the fabricated material volume under the same diffuse lighting and beam light.

Abstract

Many real world surfaces exhibit translucent appearance due to subsurface scattering. Although various methods exist to measure, edit and render subsurface scattering effects, no solution exists for manufacturing physical objects with desired translucent appearance. In this paper, we present a complete solution for fabricating a material volume with a desired surface BSSRDF. We stack layers from a fixed set of manufacturing materials whose thickness is varied spatially to reproduce the heterogeneity of the input BSSRDF. Given an input BSSRDF and the optical properties of the manufacturing materials, our system efficiently determines the optimal order and thickness of the layers. We demonstrate our approach by printing a variety of homogenous and heterogenous BSSRDFs using two hardware setups: a milling machine and a 3D printer.

1 Introduction

Traditional printing technology can reproduce the colors of natural images, but it ignores the directionally dependent aspects of real-world surface appearance. Recently, Matusik et al. [2009] demonstrated that by combining several inks with different reflectance properties, printers can reproduce the directionally dependent behavior of spatially-varying opaque materials. Another important aspect of surface appearance is subsurface scattering, which is important for translucent materials such as wax, marble, food, and skin. Although many methods have been proposed for capturing, rendering and editing subsurface scattering effects, no system exists for fabricating physical objects with such appearance.

Fabricating a material volume with desired subsurface scattering effects is useful in many applications. In the food industry, great

effort is made to manufacture realistic-looking fake food for exhibition and advertisements. Artists need powerful techniques for mimicking realistic human skin in wax sculptures. Interior designers use faux painting to reproduce the appearance of marble for surface decoration. Although dedicated techniques have been developed for many of these applications, there is no general and automatic solution for fabricating a material volume with desired translucent effects. Lots of manual work and experience are needed for crafting materials with desired translucent appearance.

In this paper, we present a method for automatically fabricating a material volume with a desired BSSRDF (bidirectional subsurface scattering reflectance distribution function) [Nicoдемus et al. 1977]. The BSSRDF is a general model for describing the surface appearance of translucent materials in terms of the light transport between every pair of surface points. We focus on optically thick materials, whose subsurface scattering behavior is well captured by the diffusion approximation [Ishimaru 1978]. For such materials, our key observation is that it is possible to reproduce the visual appearance of a given material by carefully combining other materials with different optical properties. Thus with a fixed set of basis manufacturing materials, we can reproduce a wide variety of heterogeneous BSSRDFs by stacking material layers whose thickness and composition vary spatially. The type of basis manufacturing materials and number of layers are constrained by the hardware setup. Given these constraints, our method computes the distribution of basis materials and spatially variant layer thicknesses so that the BSSRDF of the output volume is as close to the target BSSRDF as possible. A surface texture layer may be used to enrich the color of the BSSRDF of the output volume when needed. Figure 1 shows an example volume manufactured with our system.

We compute the optimal layer layout of the output volume, i.e., the distribution of basis materials and thickness of each layer, by searching for the BSSRDF that is the closest to the input BSSRDF among the space of BSSRDFs of all possible layer layouts. For a homogeneous material, the material and thickness is constant within each layer but may vary across layers. In this case, the computation is relatively easy and to further facilitate this computation we have developed an efficient method for quickly constructing the BSSRDFs of all layer layouts. The case of heterogeneous materials is much harder. The complex interactions between the optical properties and spatial distributions of the materials lead to non-linear relationship between the BSSRDF over the surface and the underlying volumetric material properties. Deriving the optimal layer

layout from the input BSSRDF is difficult as it amounts to solving a large non-linear optimization problem. Furthermore, manufacturing constraints impose limits on valid material distributions and thickness of layers and make this non-linear optimization even more challenging. We solve this problem in two steps. In the first step, we decouple the non-local BSSRDF into local scattering profiles and determine the material composition (i.e. the basis material in each layer) under each surface point with the scattering profile defined on each point separately. After that, we model the light transport between surface points using a diffusion process and optimize the thickness of the layers at each location using an adapted inverse diffusion optimization. For any given BSSRDF, our approach automatically computes the optimal material volume in dozens of minutes.

We have experimented with two hardware setups having different tradeoffs: a milling machine and a 3D printer. The milling machine allows us to choose manufacturing materials with a variety of scattering properties, but has limitations in the number and precision of the layers it can effectively produce. The 3D printer allows us to print quickly a larger number of layers with high precision, but has very limited selection of manufacturing materials. With these hardware setups, our method can generate material volumes with a wide range of homogeneous and heterogeneous BSSRDFs.

2 Related Work

Subsurface Scattering Modeling: Subsurface scattering can be described by the *bidirectional surface scattering reflectance distribution function* (BSSRDF) that expresses the light transport between pairs of surface points [Nicolodemus et al. 1977]. Many methods have been developed for capturing BSSRDFs from real materials [Debevec et al. 2000; Goesele et al. 2004; Tong et al. 2005; Peers et al. 2006], editing the measured BSSRDFs [Xu et al. 2007; Wang et al. 2008b; Song et al. 2009], and rendering BSSRDFs under different lighting conditions [Lensch et al. 2003; Hao and Varshney 2004; Wang et al. 2005; d’Eon et al. 2007]. Although these methods provide good solutions for modeling and rendering surface appearance caused by subsurface scattering, they all ignore the material properties inside the object volume. On the contrary, our system takes the BSSRDF as input and approximates its behavior with a man-made material volume.

The subsurface scattering of a translucent material can also be modeled by radiative light transfer in the material volume with known optical properties [Hanrahan and Krueger 1993; Dorsey et al. 1999; Pharr and Hanrahan 2000]. Jensen et al. [2001] presented an analytic dipole model for subsurface scattering in homogeneous translucent materials, which is then extended for modeling light diffusion in multi-layered translucent materials [Donner and Jensen 2005]. Stam [1995] modeled the light transport in heterogeneous participating media with the diffusion approximation. In [Chen et al. 2004], heterogeneous subsurface scattering is modeled with a shell texture layer and a homogeneous core, where the material properties in the volume are specified by the user. Recently, [Donner et al. 2009] presented an empirical BSSRDF model for fitting the directional BSSRDF of homogeneous materials. Different from these methods that focus on computing the subsurface scattering from known volumetric material properties, our method computes a layered volume of basis materials based on surface appearance.

Material Property Acquisition: Jensen et al. [2001] fitted the scattering properties of a homogeneous material from the BSSRDF captured from its surface. For heterogeneous translucent materials, several methods compute the spatially varying scattering properties by fitting the dipole model to BSSRDFs at each point [Tariq et al.

2006; Donner et al. 2008] or per region [Weyrich et al. 2006; Ghosh et al. 2008]. However, these methods can only represent materials with slowly varying properties such as skin, where the input BSSRDF can be well approximated by a homogeneous BSSRDF computed from scattering properties at each point. It cannot be used for modeling many other heterogeneous translucent materials with sharp variations, such as marble and jade.

In medical imaging, optical tomography [Arridge and Schotland 2009] has been developed for estimating material properties in body tissues from measured surface appearance by solving an inverse diffusion problem. [Wang et al. 2008a] presented a GPU-based inverse diffusion algorithm for computing volumetric material properties from a measured BSSRDF. Although these inverse diffusion methods can reconstruct the material properties in the object volume well, they cannot be directly applied to design the new volumetric distribution of basis materials for approximating the measured surface appearance, where the number of basis materials is limited and the scattering properties of basis materials are always different from the volumetric material properties under the measured surface. In this paper, we extend the approach in [Wang et al. 2008a] substantially, to compute a material volume suitable for manufacturing.

Appearance Printing: A traditional color printing system can faithfully print the color of surfaces, but cannot reproduce the directional dependence aspect of appearance. Weyrich et al. [2009] used a milling machine to fabricate a designed microfacet pattern on a physical surface for generating custom surface reflectance. Most recently, Matusik et al. [2009] developed a system for printing spatially varying BRDFs via a set of inks with known BRDFs. Although these systems can well reproduce the surface reflectance, they cannot model the subsurface scattering effects caused by light transport inside the object volume.

Concurrent to our work, Hašan et al. [2010] propose a 3D printer based solution for reproducing material volume with a specified BSSRDF. Although both approaches are based on the diffusion approximation and approximate the input BSSRDF with layers of basis materials, they are different in several ways. To find the layer layout for approximating homogeneous BSSRDFs, [Hašan et al. 2010] develops efficient search heuristics by pruning the layer layouts that yield poor solutions, while our paper presents a cluster based approach for computing the BSSRDFs of all valid layer layouts. This allows us to precompute the gamut of basis materials and then find the layer layout for a specified BSSRDF via nearest neighbor search. For heterogeneous BSSRDFs, [Hašan et al. 2010] determines the layer layout for each surface point separately from the local scattering profiles that are factorized from the input BSSRDF as in [Song et al. 2009]. In our method, the local scattering profiles are only used to initialize the layer layout in the volume. A volume optimization algorithm is proposed to further optimize the volume layer layout for approximating the input BSSRDF. Combined with surface texture layer and two hardware solutions (3D printer and milling machine), our method can effectively reproduce a wide variety of heterogeneous BSSRDFs with a fixed set of basis manufacturing materials.

Object Manufacturing: Most traditional computer aided design and manufacturing systems represent 3D shape with B-rep geometry [Baumgart 1972] and fabricate each separate part of a 3D shape with one homogeneous substrate. The material variation inside the object volume is ignored. 3D printers construct the complex 3D objects by aggregating materials layer by layer. Despite their hardware capability to support voxel-based object and material variations in the object volume, most commercial systems available now can only print B-rep geometry with one or two proprietary materials inside [Vilbrandt et al. 2008]. Some printers such as the Z Corp Spectrum Z510 have the capability to print colors at any voxel in an

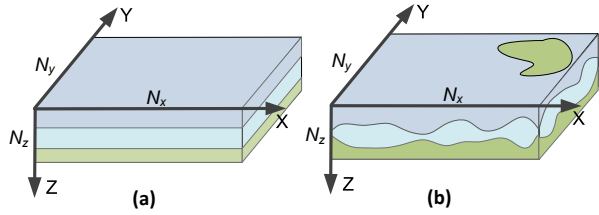


Figure 2: The output volume V . Different colors indicate layers with different basis materials. (a) The layered volume for a homogeneous BSSRDF. (b) The layered volume for a heterogeneous BSSRDF.

object volume. However, the basis materials available for printing are very limited and almost opaque.

Our system models the output volume as a set of layers of basis materials, each of which can be well converted to a B-rep geometry and fabricated by traditional manufacturing hardware (such as milling machines or 3D printers). It also can be easily extended for future 3D printing systems that support more materials and flexible material variations in the object volume.

3 System Pipeline

Input BSSRDF: The goal of our work is to approximate the appearance of a desired subsurface scattering material that is described by the BSSRDF $S(\mathbf{x}_i, \omega_i; \mathbf{x}_o, \omega_o)$ [NICODEMUS et al. 1977], which relates the outgoing radiance $L(\mathbf{x}_o, \omega_o)$ at a point \mathbf{x}_o in direction ω_o to the incoming radiance $L(\mathbf{x}_i, \omega_i)$ as

$$L(\mathbf{x}_o, \omega_o) = \int_A \int_{\Omega} S(\mathbf{x}_i, \omega_i; \mathbf{x}_o, \omega_o) L(\mathbf{x}_i, \omega_i) (\mathbf{n}(\mathbf{x}_i) \cdot \omega_i) d\omega_i d\mathbf{x}_i, \quad (1)$$

where Ω is the hemisphere around \mathbf{x}_i ; A is the area around the point \mathbf{x}_o , and $\mathbf{n}(\mathbf{x}_i)$ is the surface normal at \mathbf{x}_i . As in [GOESELE et al. 2004; PEERS et al. 2006; SONG et al. 2009], we decompose the light transport into two components as $L(\mathbf{x}_o, \omega_o) = L_s(\mathbf{x}_o, \omega_o) + L_d(\mathbf{x}_o, \omega_o)$, where $L_s(\mathbf{x}_o, \omega_o)$ accounts for light immediately reflected from the surface and L_d accounts for light scattered in the material volume. In this work, we focus on the latter component L_d that is captured by the *diffuse BSSRDF* S_d , which we further decompose as

$$S_d(\mathbf{x}_i, \omega_i; \mathbf{x}_o, \omega_o) = \frac{1}{\pi} F_r(\eta(\mathbf{x}_i), \omega_i) R_d(\mathbf{x}_i, \mathbf{x}_o) F_r(\eta(\mathbf{x}_o), \omega_o), \quad (2)$$

where F_r is the angular dependent Fresnel function that is determined by the refraction index η of the material, while R_d is a four dimensional function of two surface locations that encodes the spatial subsurface scattering of heterogeneous materials. Again following [GOESELE et al. 2004; PEERS et al. 2006; SONG et al. 2009], we focus exclusively on a representation for the 4D spatial component of the diffuse BSSRDF R_d and ignore the angular dependencies.

Output Volume: We simulate the appearance of the input BSSRDF by printing an object volume V . Different manufacturing hardware can construct objects using a fixed set of basis materials (with given translucent properties) specific to that hardware. To approximate the BSSRDF on the surface, we construct the volume with layers of these basis materials, as shown in Figure 2. The thickness of layers under each surface point is identical for homogeneous BSSRDFs, and varied appropriately for simulating heterogeneous BSSRDFs. To model a BSSRDF with sharp variations, the basis materials in the layer may also be varied under each surface point. In our experiments, we found that to ensure that the output volume is not too fragile, the minimal thickness of material layers needs to be limited. Furthermore, to save manufacturing time and cost, we also limit the total number of layers in the output volume.

Said another way, 3D manufacturing methods impose *layout constraints* that we have to respect during printing.

Material Mapping: As in standard printing methods, the output volume is just an approximation of the input BSSRDF. Given the basis materials and layout constraints, our goal is to produce an output volume that is as close to the original input as possible. We call *material mapping* the process by which we determine the volume to print. More formally, while respecting layout constraints, we seek to minimize the L^2 difference E between the input BSSRDF R_d and output BSSRDF R'_d of the printed volume V , written as

$$E = \int_{\mathbf{x}_i} \int_{\mathbf{x}_j} \|R_d(\mathbf{x}_i, \mathbf{x}_j) - R'_d(\mathbf{x}_i, \mathbf{x}_j)\|^2 d\mathbf{x}_i d\mathbf{x}_j. \quad (3)$$

To print the volume, we need to determine the basis material and thickness of each layer, which we call the *layer layout*, under each surface point in the volume V . Since the surface BSSRDF depends on the volume distribution in a non-linear manner, determining the layer layouts for the volume V amounts to a non-linear optimization. This makes BSSRDF printing very different from color and reflectance printing, since in those cases determining what to print amounts to simpler operations.

To print homogeneous materials, we map the BSSRDF to a volume made by layering slabs of homogeneous basis materials that have the same thickness for points on the surface. Conceptually, to determine the basis material and the thickness of each layer, we compute the BSSRDF for all possible layer layouts, generated by the basis materials, and pick the closest one. Since computing the BSSRDF for each layer layout by brute force is expensive, we develop an efficient method for quickly constructing the BSSRDFs of all layer layouts.

To print a BSSRDF generated from heterogeneous translucent materials, we vary the column layer layouts under different surface points in the output volume. The resulting light transport becomes more complex due to the heterogeneity, making material mapping more challenging. We make this process manageable by introducing a two step process. First, in the *volume initialization step*, we factor the BSSRDF into local scattering profiles. We then approximate each scattering profile with a homogeneous BSSRDF and initialize the layer layout (i.e. the basis material and thickness of each layer) in each column separately with the homogeneous mapping method. At each surface point, this initialization determines the basis material for each layer and a starting layer thickness. We use this as starting configuration for a second step, the *volume optimization step*, where we model the light transport in the volume using a diffusion process and optimize the thickness of the layers at each location using an adapted inverse diffusion optimization [WANG et al. 2008a]. We will describe the details of our material mapping procedure in the following sections.

Surface Texture: Since we use only a small number of basis materials with limited color hues and saturations, it is possible that some of the rich chromatic variations in input BSSRDFs falls outside the color gamut of our basis. To further enrich the color of the BSSRDF generated by the output volume, a very thin color texture layer is placed on the top surface for modulating both incoming and outgoing radiance. We ignore the thickness of this color texture layer and represent it as a $N_x \times N_y$ 2D surface color texture T that represents the transmission for RGB channels, in which 1 indicates fully transparent and 0 is opaque. Given input BSSRDF R_d , we solve the optimal color texture and the output volume iteratively. Given the initial color texture T_0 , we modulate the input BSSRDF $R_d(\mathbf{x}_i, \mathbf{x}_o)$ as $R'_d(\mathbf{x}_i, \mathbf{x}_o) = R_d(\mathbf{x}_i, \mathbf{x}_o) / (T(\mathbf{x}_i)T(\mathbf{x}_o))$ and use the re-

σ_s	(1,12, 1,12, 1,13)	(5,47, 5,53, 5,37)	(0,52, 0,53, 0,58)	(3,12, 3,31, 3,37)	(1,21, 1,35, 1,45)
σ_a	(0,052, 0,053, 0,045)	(0,003, 0,003, 0,004)	(0,001, 0,001, 0,001)	(0,007, 0,007, 0,006)	(0,002, 0,002, 0,016)
	(a)	(b)	(c)	(d)	(e)

Figure 3: Photographs and optical properties of basis materials used in our two manufacturing solutions. (a)(b)(c) The basis materials used for the milling machine solution. (d)(e) The basis materials used for the 3D printer solution.

result R_d^T as the input for material mapping. After material mapping, we update the color texture by

$$T(\mathbf{x}) = \frac{\sum_{\mathbf{x}_o \in A} R_d(\mathbf{x}, \mathbf{x}_o)^2 R_d'(\mathbf{x}, \mathbf{x}_o)}{\sum_{\mathbf{x}_o \in A} R_d(\mathbf{x}, \mathbf{x}_o)}, \quad (4)$$

where R_d' is the BSSRDF computed from the output volume obtained by material mapping. We repeat this process until the update of the color texture is small enough.

Manufacturing Hardware: We tested our system with two manufacturing configurations. The first solution is based on a milling machine, where the basis material for each layer can be chosen from a set of substrates with different translucency and colors. We mill each material layer separately from a substrate block and assemble all layers together to generate the output volume. We use three basis materials and limit the number of layers to three for this hardware.

The second solution is based on a 3D printer, which can print complex geometric shapes with high precision. Our 3D printer provides one basis material used to print 3D shapes and one support material that is used during the printing process, but normally removed after printing. In our system, we retain the support material after printing and use it as a second basis material. We use six layers for this hardware. Figure 3 illustrates all basis materials and their scattering properties in these two solutions.

Printing Gamut: It is surprising that given this small number of basis materials, the resulting output volumes we generate approximate well a wide range of BSSRDFs. We borrow the term ‘‘gamut’’ from traditional printing to indicate the space of homogenous BSSRDFs reproduced by our setup. Figure 4 shows the gamut of our two manufacturing setups, where σ_s and σ_a are the scattering coefficient and absorption coefficient of the homogenous material, respectively. We compute this gamut by mapping each homogenous BSSRDF to a layered volume of basis materials and include in the gamut all BSSRDFs with relative mapping errors smaller than 10^{-4} . We compute the relative error as

$$\frac{\int_{\mathbf{x}_i} \int_{\mathbf{x}_j} \|R_d(\mathbf{x}_i, \mathbf{x}_j) - R_d'(\mathbf{x}_i, \mathbf{x}_j)\|^2 d\mathbf{x}_i d\mathbf{x}_j}{\int_{\mathbf{x}_i} \int_{\mathbf{x}_j} \|R_d(\mathbf{x}_i, \mathbf{x}_j)\|^2 d\mathbf{x}_i d\mathbf{x}_j}. \quad (5)$$

Different from material and reflectance printing, the gamut of homogenous materials we can simulate is larger than the convex hull of the basis materials. This is the result of the non-linear relationship between the BSSRDF and the volumetric material properties. From an intuitive standpoint, since an observer can only see the object surfaces, we are free to vary the volume as needed to reproduce that appearance.

Computing all the possible heterogeneous BSSRDFs that can be reproduced by our setup is prohibitively expensive. To gain an intuition of which heterogeneous variations we can reproduce, we make the observation that heterogeneous BSSRDFs can be factored into products of 1D scattering profiles independently defined at each surface location [Song et al. 2009]. These scattering profiles rep-

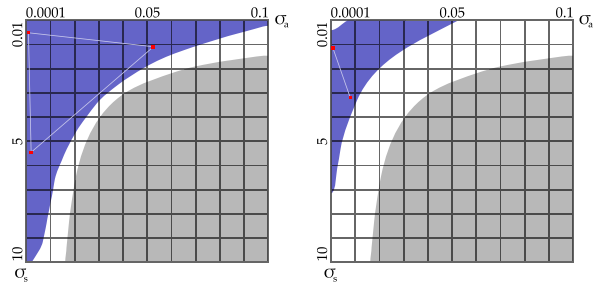


Figure 4: The gamuts of our two manufacturing setups. The basis materials are indicated by red points. The blue gamut regions indicate the homogeneous materials whose BSSRDFs can be reproduced by our setup. The grey regions mark the homogeneous materials with little scattering (with BSSRDF radius smaller than 1.0mm), which are not the main targets of our method. (a) The gamut of three basis materials used for the milling machine solution. (b) The gamut of two basis materials used for the 3D printer solution.

resent well the local scattering effects at each surface location, effectively decoupling the pairwise correlations in the heterogeneous BSSRDF. Intuitively, at each surface location we can think of the scattering profile as approximately defining a homogenous BSSRDF that describes scattering from a small homogenous region around the point. If all these homogenous BSSRDFs fit within our gamut, our material volume should approximate well the original heterogeneous BSSRDF.

4 Material Mapping

Volume Representation: In this section we discuss the details of how we compute the output volume that best matches the input BSSRDF. In our algorithms, the volume V is represented as $N_x \times N_y \times N_z$ voxels on a regular 3D grid, where $N_x \times N_y$ determines the surface resolution and N_z determines the thickness of the layered material volume (Figure 2). The voxel size is set to the precision of the manufacturing hardware along three axes. The volume is composed by N_l layers, each made of one of the basis materials. We discretize each layer thickness by the voxel size and limit it to be larger than a minimal thickness determined by the manufacturing hardware. We indicate with M_x the *layer layout* under a surface point \mathbf{x} , defined as the set of basis materials and thickness for each layer in the column under \mathbf{x} .

4.1 Homogeneous BSSRDFs

Output Volume: Let us first consider the BSSRDF generated from a semi-infinite homogeneous material slab, which is isotropic and can be represented as a function of distance $r = \|\mathbf{x}_i - \mathbf{x}_o\|$ between two surface points as $R(r) = R_d(\mathbf{x}_i, \mathbf{x}_o)$. To reproduce this BSSRDF, we layer N_l slabs of base materials that have equal thickness for all points on the surface. The resulting multi-layered volume is homogenous along the X and Y directions but heterogeneous along Z.

Homogenous Mapping: To determine the basis material and thickness of each layer (i.e. the number of voxels it occupies along Z), we solve Equation 3 by computing the BSSRDFs for all possible layer layouts of the basis materials, and pick the closest one to the input BSSRDF.

For each configuration, we compute the BSSRDF $R_{N_l}(r)$ generated by the volume with Kubelka-Munk theory [Donner and Jensen

2005]:

$$\hat{R}_{N_l} = \hat{R}_1 + \frac{\hat{T}_1 \hat{R}_1 \hat{T}_1}{1 - \hat{R}_1 \hat{R}_{N_l-1}} \quad (6)$$

where \hat{R} and \hat{T} refer to the Fourier transformed function $R(r)$ and $T(r)$. $R_1(r)$ and $T_1(r)$ are the BSSRDF and transmission function of the top layer computed using the multipole model [Donner and Jensen 2005]. $R_{N_l-1}(r)$ is the BSSRDF of the remaining $N_l - 1$ layers beneath the top layer, which can be recursively computed using Equation 6. After computation, we transfer the result back to the spatial domain via inverse FFT.

Performing this computation for each layer layout separately would be impractical given the very large number of possible configurations. We reduce the number of needed BSSRDF evaluations by observing that many layer layouts of basis materials generate similar BSSRDFs. This is because small variations of layer thickness generally have little effect on a BSSRDF. Therefore, for layer layouts that have the same top layer and similar $R_{N_l-1}(r)$, we can compute their BSSRDF once.

Based on this observation, our algorithm starts by constructing the set $M^1 = \{m^1\}$ of all layouts m^1 that include a single basis material whose thickness is varied from the minimal layer thickness to the output volume thickness in voxel sized steps along Z. We compute the BSSRDFs and transmission functions of each slab using the multipole model [Donner and Jensen 2005]. We then cluster these layouts using k-means clustering such that the distance of BSSRDFs in each cluster is less than a small threshold. For each cluster, we compute the representative BSSRDF and transmission function as the average of BSSRDFs and transmission functions of layer layouts in the cluster.

After that, we iteratively construct all layer layouts from bottom to top in N_l steps. In each step, we generate the set M^{i+1} of candidate layouts constructed by adding a basis material layer m_l^i from M^1 to a layer layout m_l^i from M^i . Formally, $M^{i+1} = \{m_l^i \cup m_l^i | m_l^i \in M^1, m_l^i \in M^i\}$, where the \cup operator adds a layer on top of a layout. We discard all layouts with thickness larger than the output volume. The BSSRDF of each layout in M^{i+1} is computed with the representative of M_l^1 and M_l^i using Equation 6. Thus the total number of BSSRDF computations is $N_{M^1} \times N_{M^i} \ll |M^1| \times |M^i|$, where N_{M^1} and N_{M^i} are the number of clusters in M^1 and M^i and $|\cdot|$ is the size of a set. We then cluster M^{i+1} based on the layout BSSRDFs and pick representatives.

After N_l steps, we remove all layer layouts whose thickness is not equal to volume thickness and compute the BSSRDF for layouts in the final set. Given an input BSSRDF, we first search for the best matched representative BSSRDF. We then compute the BSSRDF of each layer layout in this cluster and search for the best match. The approximate nearest neighbor acceleration scheme is used to speed up this search process [Mount and Arya 1997].

4.2 Heterogeneous BSSRDFs

Overview: To print a BSSRDF generated from heterogeneous translucent materials, we vary the column layer layouts (i.e. the basis material and thickness in each layer) under different surface points, resulting in a heterogeneous output volume. Computing the layer layouts for each column amounts to solving the non-linear optimization problem defined in Equation 3. This optimization is much more challenging than homogeneous mapping since the BSSRDF of a heterogeneous output volume is determined by the couplings of different layer layouts in all columns. We do so with a two step process. First, in the *volume initialization step*, we decouple the BSSRDF into local scattering profiles and use the homogenous

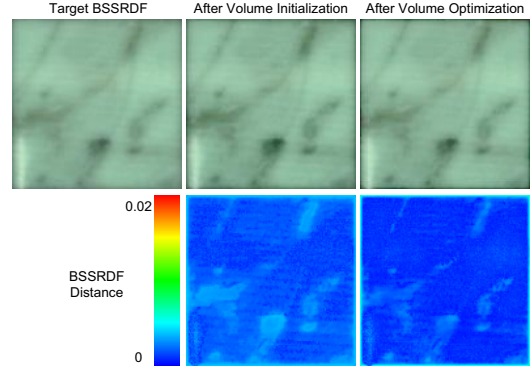


Figure 5: Rendering results of BSSRDFs after volume initialization and volume optimization under diffuse lighting shown in the top row. The errors of BSSRDFs after the initialization and optimization processes are presented in the bottom row.

algorithm in Section 4.1 to assign basis materials and initial layer thickness to each column separately. Second, in the *volume optimization step*, we then optimize all layer thickness for all columns concurrently by using an inverse diffusion optimization. Figure 5 shows the best fit volume after each step compared to the original BSSRDF. After initialization, the layered material volume roughly approximates the input BSSRDF. Further improvements to the approximation are achieved with volume optimization.

Scattering Profiles: To determine the material layout in each column, we first decouple the input diffuse BSSRDF R_d into a product of 1D scattering profiles $P_x(r)$ defined at each surface location \mathbf{x} , and parameterized over the local distance $r = \|\mathbf{x}_o - \mathbf{x}_i\|$ as in [Song et al. 2009]: $R_d(\mathbf{x}_i, \mathbf{x}_o) \approx \sqrt{P_x(r)} P_{x_o}(r)$. For a heterogeneous BSSRDF, this factorization effectively decouples the non-local light transport between pairs of surface points into a set of local scattering profiles, each of which is defined at a single point and mainly determined by the scattering properties of the material volume under such a surface point.

Volume Initialization: Based on this observation, we consider the homogenous BSSRDF determined by the scattering profile at each location \mathbf{x} , defined as $R_x(r) = \operatorname{argmin}_R \int_0^\infty [P_x(r) - R(r)]^2 r dr$, and use the homogenous algorithm presented above to assign a layer layout for the material column at \mathbf{x} . More specifically, we first precompute the BSSRDFs of all valid homogenous layer layouts. For each surface location, we then search for the best matching representative BSSRDF in the precomputed dataset. We then choose the layer layout in this cluster that is most similar to the ones assigned to the neighboring points, proceeding in scanline order. To assign a layer layout to the point, the similarity of layer layouts is measured by $\sum_z \delta(b_x(z), b_y(z))$ where $b_x(z)$ and $b_y(z)$ are the basis materials at depth z for the layer layouts at x and y . This assignment scheme favors smoothly varying layer layouts for regions with similar local scattering profiles.

The initialized volume only provides a rough approximation for the input BSSRDF because the light transport between columns is not considered in the last step. To obtain a better match, we fix the basis materials used in all layers and further optimize all layer thicknesses concurrently to better approximate the input BSSRDF by minimizing the objective function in Equation 3. Here the BSSRDF of the output volume R'_d is computed by simulating the light transport in the volume with a diffusion process, which is described by the following equations for points \mathbf{v} in the volume V and points \mathbf{x} on the surface A [Ishimaru 1978; Arbre 2009]:

$$\nabla \cdot (\kappa(\mathbf{v}) \nabla \phi(\mathbf{v})) - \sigma_a(\mathbf{v}) \phi(\mathbf{v}) = 0, \quad \mathbf{v} \in V \quad (7)$$

Set basis materials for each layer using the <i>volume initialization step</i>
Set initial thicknesses \mathbf{h}_0 using the <i>volume initialization step</i>
Set initial search direction: $\mathbf{d}_0 = -\nabla E_h(\mathbf{h}_0)$ and $\mathbf{p}_0 = \mathbf{d}_0$
Repeat following steps until $E_h < \epsilon$
Compute gradient: $\nabla E_h(\mathbf{h}_t) = \left(\frac{dE_h}{d\mathbf{h}(\mathbf{x}, l)} \right)$
Set $\mathbf{p}_t = -\nabla E_h(\mathbf{h}_t)$
Update search direction: $\mathbf{d}_t = \mathbf{p}_t + \beta \cdot \mathbf{d}_{t-1}$, $\beta = \max\left(\frac{\mathbf{p}_t^T (\mathbf{p}_t - \mathbf{p}_{t-1})}{\mathbf{p}_{t-1}^T \mathbf{p}_{t-1}}, 0\right)$
Compute λ : Golden section search by $\min_{\lambda} [E_h(\mathbf{h}_t + \lambda \mathbf{d}_t)]$
Update solution $\mathbf{h}_{t+1} = \mathbf{h}_t + \lambda' \mathbf{d}_t$

Table 1: Conjugate gradient based algorithm for minimizing E_h .

$$\phi(\mathbf{x}) + 2c\kappa(\mathbf{x}) \frac{\partial \phi(\mathbf{x})}{\partial \mathbf{n}(\mathbf{x})} = \frac{4}{1 - F_{dr}} L_i(\mathbf{x}) \quad \mathbf{x} \in A \quad (8)$$

where $\sigma_a(\mathbf{v})$ and $\kappa(\mathbf{v}) = 1/[3(\sigma_a(\mathbf{v}) + \sigma_s(\mathbf{v}))]$ denote the absorption and diffusion coefficients at \mathbf{v} , $\phi(\mathbf{v})$ is the radiant flux, F_{dr} is the diffuse Fresnel reflectance (determined by the refraction index η of the material [Jensen et al. 2001]) and $c = (1 + F_{dr})/(1 - F_{dr})$. Here we assume the phase function of the material is isotropic. The diffuse incoming lighting $L_i(\mathbf{x})$ at a surface point \mathbf{x} is given by $L_i(\mathbf{x}) = \int_{\Omega} L(\mathbf{x}, \omega_i)(\mathbf{n} \cdot \omega_i) F_r(\eta(\mathbf{x}), \omega_i) d\omega_i$. Once the radiant flux is determined for a given incoming lighting by the diffusion process, the multiple scattering component of the outgoing radiance at \mathbf{x} is computed as

$$L_d(\mathbf{x}, \omega_o) = \frac{F_r(\eta(\mathbf{x}), \omega_o)}{4\pi} \left[\left(1 + \frac{1}{c}\right) \phi(\mathbf{x}) - \frac{4}{1 + F_{dr}} L_i(\mathbf{x}) \right]. \quad (9)$$

We can then compute the diffuse BSSRDF between two surface points, by considering a unit incoming lighting $L_i(\mathbf{x}) = 1$ at \mathbf{x} and ignoring the angular Fresnel terms for both incoming and outgoing lighting, as

$$R'_d(\mathbf{x}_i, \mathbf{x}_o) = \begin{cases} \frac{1}{4\pi} \left[\left(1 + \frac{1}{c}\right) \phi(\mathbf{x}_o) \right] & \mathbf{x}_i \neq \mathbf{x}_o \\ \frac{1}{4\pi} \left[\left(1 + \frac{1}{c}\right) \phi(\mathbf{x}_o) - \frac{4}{1 + F_{dr}} \right] & \mathbf{x}_i = \mathbf{x}_o. \end{cases} \quad (10)$$

We determine the thickness of each layer by minimizing the objective function in Equation 3 where the volume BSSRDF is computed using the diffusion process above. This can be solved by inverse diffusion optimization, as in [Wang et al. 2008a]. Since the basis materials in all layers are determined during initialization, the objective function E_h is a function of only the set of spatially varying layer thicknesses $\mathbf{h} = \{h(\mathbf{x}, l)\}$, where $h(\mathbf{x}, l)$ is the starting depth of layer l at \mathbf{x} .

To minimize E_h , we apply the conjugate gradient algorithm, summarized in Table 1. We begin by initializing basis materials and layer thickness using the homogenous method. At each step, we determine the gradient ∇E_h of E_h with respect to \mathbf{h} . To guarantee that the thickness is larger than the minimal layer thickness defined by the material configuration, we set the gradient to 0 when the thickness reaches the minimal thickness constraint. The search direction is then updated with the Polak-Ribiere method [Press et al. 1992]. The optimal step size λ along the search direction is found by a golden section search. We then update \mathbf{h} using the computed gradient ∇E_h and λ . We continue iterating until the layer thickness converges.

Gradient Computation: The most expensive step of this algorithm is the computation of the E_h gradient relative to the thicknesses $h(\mathbf{x}, l)$. A straightforward method is to perturb each layer boundary at each location, update the material properties in the volume, and compute the resulting change in objective function value. This would require $N_x \times N_y \times N_l$ diffusion simulations, becoming prohibitively expensive. We speed up this procedure by using an adjoint method similar to [Wang et al. 2008a].

We represent the error $E_h(\{\kappa\}, \{\sigma_a\})$ as a function of the material properties κ and σ_a of all voxels in the volume. Since these are

in turn defined by the layer thickness (and the basis materials fixed during optimization), we can use the chain rule to derive the gradient of the objective function relative to layer thickness as:

$$\frac{dE_h}{dh(\mathbf{x}, l)} = \frac{dE_h}{d\kappa(\mathbf{x}, z_l - 1)} \frac{d\kappa(\mathbf{x}, z_l - 1)}{dh(\mathbf{x}, l)} + \frac{dE_h}{d\sigma_a(\mathbf{x}, z_l - 1)} \frac{d\sigma_a(\mathbf{x}, z_l - 1)}{dh(\mathbf{x}, l)} \quad (11)$$

where (\mathbf{x}, z_l) refers to the first voxel in the l -th layer at \mathbf{x} , and $(\mathbf{x}, z_l - 1)$ is the last voxel of upper $l - 1$ layers. Note that this computation only involves voxels at the layer boundaries because the change of the layer boundary only modifies the material properties in the boundary voxels. We compute $dE_h/d\kappa(\mathbf{x}, z_l - 1)$ and $dE_h/d\sigma_a(\mathbf{x}, z_l - 1)$ using the adjoint method (see Appendix for details) [Wang et al. 2008a], while $d\kappa(\mathbf{x}, z_l - 1)/dh(\mathbf{x}, l)$ and $d\sigma_a(\mathbf{x}, z_l - 1)/dh(\mathbf{x}, l)$ are directly computed by

$$\begin{aligned} \frac{d\kappa(\mathbf{x}, z_l - 1)}{dh(\mathbf{x}, l)} &= \kappa(\mathbf{x}, z_l) - \kappa(\mathbf{x}, z_l - 1) \\ \frac{d\sigma_a(\mathbf{x}, z_l - 1)}{dh(\mathbf{x}, l)} &= \sigma_a(\mathbf{x}, z_l) - \sigma_a(\mathbf{x}, z_l - 1). \end{aligned} \quad (12)$$

Using this scheme, we only need two diffusion simulations for computing the gradient, which is much more efficient than the straightforward method.

Diffusion Computation: In inverse diffusion optimization, the diffusion simulation is used in both gradient computation and golden search. To solve the diffusion equation on a 3D regular grid of a layered material volume, we discretize the diffusion equation as a set of linear equations over the voxels using the finite difference method (FDM) scheme in [Stam 1995]. We implemented a multigrid method [Press et al. 1992] for solving this sparse linear system on the GPU using CUDA. The adjoint diffusion equation is discretized and computed in the same way.

5 Hardware Manufacturing Setup

We fabricate the output volume determined during material mapping using two different hardware solutions: a milling machine and a 3D printer.

Milling Machine: The first solution is based on an Atrump M218 CNC machining center. The maximum operating range is 660mm, 460mm, and 610mm in the X, Y and Z directions respectively. The stepper motor resolution is 0.005mm. The machining center has an automation tool changer with 16 drill bits. The size of drill bits ranges from 6mm to 0.5mm. Based on these hardware properties, we set the output volume size to be 130mm along each dimension, and the voxel size is $1.0\text{mm} \times 1.0\text{mm} \times 0.1\text{mm}$, so one pixel of the measured BSSRDF corresponds to one voxel of the output volume. The number of layers in the volume is three and the minimal layer thickness is 1.0mm.

Given the output volume, we convert each layer into a B-rep and fabricate it with the milling machine. If both sides of a layer are not flat, our system splits it into two or more pieces, each of which has one flat side. For all results shown in this paper, we only need to split the middle layer into two pieces for manufacturing. Given the B-rep of each layer piece, the milling machining center mills a basis material block into our desired layer shape. A typical output of the milling machine is shown in Figure 1. After the milling process, we use UV sensitive glass glue to assemble those layers into the final volume and ignore the light refraction between the layer boundaries. The milling time varies with the complexity of the layer surface. For the homogeneous cases, the average total milling time for all three layers is about 30 minutes. For the heterogeneous cases, the total milling time ranges from one hour to six hours.

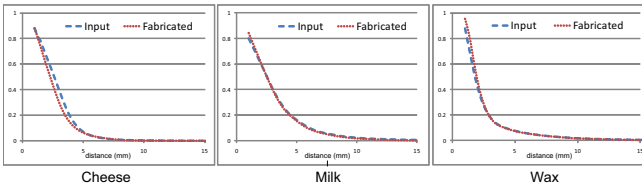


Figure 6: The comparisons of the red channel scattering profiles measured from the real homogeneous material samples (in blue) and the ones measured from the fabricated volumes (in red).

In our implementation, we use the Mastercam software to execute GCode to control the milling process. We do not optimize the smoothness of the layer thickness of neighbor columns as in [Weyrich et al. 2009] because the voxel size along the X and Y directions in our setup is larger than the mill bit diameters. Moreover, our solution is not sensitive to the layer surface orientation. In practice, we found that the milling machine can reproduce well our desired layer shapes without visual artifacts in the final results.

3D Printer: The second solution is based on an Object Eden250 3D printing system. The net build size is $250\text{mm} \times 250\text{mm} \times 200\text{mm}$, and the precision of the resulting volume is 0.1mm along each dimension. Thus we set the output volume size to be $100\text{mm} \times 100\text{mm} \times 30\text{mm}$ and 0.1mm as the voxel size. The minimal layer thickness is 0.1mm in this setup. Since the printer can control the material distribution in more flexible way, we set the number of layers to six in the output volume. For this solution, one pixel of the measured BSSRDF corresponds to 10×10 voxels of the fabricated volume. We obtain the BSSRDF for each voxel by upsampling the original BSSRDF.

The printer manufactures objects with a single resin. It prints the 3D shapes with the resin material, while the support substrate automatically fills the vertical gaps between the resins and the vertical gaps between the resin and the build tray. Therefore, we convert the layers consisting of resin materials as B-rep shapes and send them together to the 3D printer. To print the volume with the support material in the top layer, we add an extra thin resin layer on top of the volume for printing and then remove it after printing. Both materials in the output volume are kept. Depending on the complexity of material distribution and output volume size, the printing time varies from 1.5 hours to 3 hours.

Basis Material Properties Measurement: For each basis material, we measure the optical properties from a thick homogeneous block of size of $100\text{mm} \times 100\text{mm} \times 64\text{mm}$, where the light transport in the volume is well modeled by the dipole approximation. We then shoot red (635nm), green (532nm) and blue laser beams (473nm) at a point on the top surface and capture the HDR images of the scattering profiles around the lighting point for each color channel. We then follow the method in [Jensen et al. 2001] to fit the material properties from the captured scattering profiles. Since the basis material blocks are not perfectly homogeneous, we randomly sampled scattering profiles at ten points on the top surface and average them to get the final scattering profile for fitting. Figure 3 lists the material properties of all basis materials used in our two hardware solutions. All the basis materials we used have a similar refractive index of 1.5. Thus in our implementation we ignore the mismatch of refractive index between layers.

Color Texture: We printed our color texture with a Canon PIXMA iP8500 ink jet printer on a transparent film. To calibrate the color, we print out a color pattern and captured a photo under uniform back lighting with a calibrated camera. Then we compute the transmission rate of the inks.

Material Samples					
Time	15 min	23 min	45 min	42 min	35 min

Table 2: Computation times for all heterogeneous BSSRDF results shown in the paper.

6 Experimental Results

Material Mapping: We have implemented our system on a Intel Xeon E5400 machine with an NVidia GeForce 9800GT graphics card. The material mapping algorithm is implemented in C++ on the CPU, while the diffusion simulation is implemented using CUDA on the GPU. The computation time for solving the volume layout of a homogeneous input BSSRDF is about 10 minutes. For all heterogeneous BSSRDF results shown in the paper, our system takes about 10 minutes for computing the printing gamut and doing volume initialization. Depending on the volume size and the number of layers in the output volume, it then takes 15 to 45 minutes for volume optimization (Table 2), in which 80% of the time is spent for golden search, 16% for gradient computation, and 4% for other computations. The number of conjugate gradient steps in the volume optimization depends on the spatial complexity of the input BSSRDF and varies across samples, ranging from 5 to 50.

Method Validation: We evaluated our method with three homogeneous BSSRDFs measured from real material samples. For this purpose, we chose three materials (cheese, milk and wax) with various degrees of translucency and simulated their homogeneous BSSRDFs with layered volumes fabricated by the milling machine. One pixel of the measured BSSRDF corresponds to 1mm of the actual size, thus the fabricated sample is $1 : 1$ scale to the real sample. No surface textures are applied to the resulting volumes. Figure 7 illustrates the scattering effects of real homogeneous material samples and fabricated material volumes under circular lighting. We measure the BSSRDF from the fabricated volume and compute its relative error by Equation 5. Figure 6 compares the scattering profiles measured from real samples to the ones measured from the fabricated results. With three basis material slabs, the fabricated volumes faithfully reproduce the homogeneous BSSRDFs with different scattering ranges.

We also tested our method with three measured BSSRDFs with different kinds of heterogeneity. Figure 8 shows the rendering results of input heterogeneous BSSRDFs with images of our output volumes under the different lightings. The two marble data sets are from [Peers et al. 2006], and the jade data set is from [Song et al. 2009]. We used the milling machine to fabricate the layered volumes for approximating the two marble data sets and used the 3D printer for generating the volume for simulating the jade BSSRDF. The surface textures are used for modulating the BSSRDFs of all three volumes. We ignored the physical size of the original sample and followed the pixel to voxel correspondence to determine the output scale (e.g. for the milling machine solution, one pixel of the measured BSSRDF corresponds to one voxel, and for the 3D printer solution, one pixel of the measured BSSRDF corresponds to 10×10 voxels of the fabricated volume) We calibrated the projector and camera used in our capturing setup and used the same lighting for rendering. As shown in Figure 8, our method effectively simulates the heterogeneous scattering effects of different materials. Please see the accompanying video for more comparison results. We scanned the volume with a line light and computed the relative errors by $E_r = \sum_i (I_i - I'_i)^2 / \sum_i (I_i)^2$, where I'_i is the image captured from the fabricated volume, while I is the rendering result of the input BSSRDF.

More Results: Figure 9 shows a fabricated material volume for simulating the heterogeneous BSSRDF of a real salmon slice. We followed the method in [Peers et al. 2006] to capture the BSSRDF from a portion of real salmon slice (i.e. the blue box in Figure 9(a)) and then used the measured BSSRDF as input to our system. We printed the output volume using the 3D printer and applied a color texture on its top surface. The size of the output volume is scaled to $100\text{mm} \times 100\text{mm} \times 12\text{mm}$, while the size of the actual salmon slice is $60\text{mm} \times 60\text{mm}$. As shown in Figure 9(c), the sharp variations of scattering effects caused by different tissues are well captured by our fabricated volume. Combined with surface texture, the resulting volume generates convincing scattering effects under different lighting. Please see the accompanying video for more results.

Using our method, the user can also fabricate arbitrary objects with convincing translucent appearance. To this end, our system first generates the layered material volume from the input BSSRDF and then maps the layered material volume to a 3D object volume via shell mapping [Porumbescu et al. 2005]. After that, we print the 3D object volume out via the 3D printer. Figure 10 displays a fabricated jello piece with translucent appearance captured from a real piece of jello. Figure 11 shows a fabricated round plate with a jade BSSRDF designed by an artist. Under different lightings, the fabricated object exhibits compelling subsurface scattering effects.

Limitations Since our method only focuses on diffuse BSSRDFs, it cannot well model subsurface scattering of very translucent materials. Surface reflectance as well as single scattering are also ignored in our approach. Moreover, due to the small number of basis materials used in our method, our method will fail to reproduce BSSRDFs with rich chromatic variations that are out of the color gamut. The surface texture used in our method alleviates this limitation but cannot totally solve it. Limited by the thickness of the output volume, our method cannot be applied for 3D objects with sharp geometry features.

7 Conclusions

We have presented a complete and efficient solution for modeling and fabricating desired spatially varying subsurface scattering effects with a limited number of basis materials. In our system, the input BSSRDF is represented by a layered volume of basis materials, which can be separated into homogeneous components and easily manufactured by existing hardware. A material mapping algorithm has been proposed for efficiently computing an optimal layered volume for an input BSSRDF. A surface texture is used to further enhance the color of the BSSRDF of the output volume. Experimental results show that our system can well reproduce a wide range of heterogeneous subsurface scattering effects.

There are several interesting directions for future work. First, we would like to investigate perceptual based distance metric for evaluating the visual similarity between the input BSSRDFs and BSSRDFs of the fabricated volumes. Second, we would like to extend our method for modeling directional BSSRDF effects such as single scattering. Finally, it would be interesting to integrate our method with other surface reflectance printing methods for manufacturing 3D objects with more realistic surface appearance.

Acknowledgements

The authors would like to thank Steve Lin for paper proofreading and Matt Callcut for video dubbing. The authors also thank Matt Bell and William B. Kerr for operating the 3D printer. The authors are grateful to the anonymous reviewers for their helpful suggestions and comments. Fabio Pellacini was supported by the NSF (CNS-070820, CCF-0746117), Intel and the Sloan Foundation.

References

- ARBREE, A. 2009. *Scalable And Heterogeneous Rendering Of Subsurface Scattering Materials*. PhD thesis, Cornell University, Ithaca, New York. <http://hdl.handle.net/1813/13986>.
- ARRIDGE, S. R., AND SCHOTLAND, J. 2009. Optical tomography: Forward and inverse problems. *Inverse Problems* 25, 12, 123010:(59pp).
- BAUMGART, B. G. 1972. Winged edge polyhedron representation. Tech. rep., Stanford, CA, USA.
- CHEN, Y., TONG, X., WANG, J., LIN, S., GUO, B., AND SHUM, H.-Y. 2004. Shell texture functions. *ACM Trans. Graph.* 23, 3, 343–353.
- DEBEVEC, P., HAWKINS, T., TCHOU, C., DUKER, H.-P., SAROKIN, W., AND SAGAR, M. 2000. Acquiring the reflectance field of a human face. In *Proc. ACM SIGGRAPH*, 145–156.
- D’EON, E., LUEBKE, D., AND ENDERTON, E. 2007. Efficient Rendering of Human Skin. *Eurographics Symposium on Rendering*, 147–157.
- DONNER, C., AND JENSEN, H. W. 2005. Light diffusion in multi-layered translucent materials. *ACM Trans. Graph.* 24, 3, 1032–1039.
- DONNER, C., WEYRICH, T., D’EON, E., RAMAMOORTHI, R., AND RUSINKIEWICZ, S. 2008. A layered, heterogeneous reflectance model for acquiring and rendering human skin. *ACM Trans. Graph.* 27, 5, 140.
- DONNER, C., LAWRENCE, J., RAMAMOORTHI, R., HACHISUKA, T., JENSEN, H. W., AND NAYAR, S. 2009. An empirical bssrdf model. *ACM Transactions on Graphics* 28, 3 (July), 30:1–30:10.
- DORSEY, J., EDELMAN, A., LEGAKIS, J., JENSEN, H. W., AND PEDERSEN, H. K. 1999. Modeling and rendering of weathered stone. In *Proc. ACM SIGGRAPH*, 225–234.
- GHOSH, A., HAWKINS, T., PEERS, P., FREDERIKSEN, S., AND DEBEVEC, P. 2008. Practical modeling and acquisition of layered facial reflectance. *ACM Trans. Graph.* 27, 5, 139.
- GOESELE, M., LENSCH, H. P. A., LANG, J., FUCHS, C., AND SEIDEL, H.-P. 2004. DISCO: acquisition of translucent objects. *ACM Trans. Graph.* 23, 3, 835–844.
- HANRAHAN, P., AND KRUEGER, W. 1993. Reflection from layered surfaces due to subsurface scattering. In *Proc. ACM SIGGRAPH*, 165–174.
- HAO, X., AND VARSHNEY, A. 2004. Real-time rendering of translucent meshes. In *ACM Trans. Graph.*, vol. 23. 120–142.
- HAŠAN, M., FUCHS, M., MATUSIK, W., PFISTER, H., AND RUSINKIEWICZ, S. M. 2010. Physical reproduction of materials with specified subsurface scattering. *ACM Transactions on Graphics* 29, 3 (Aug.).
- ISHIMARU, A. 1978. *Wave Propagation and Scattering in Random Media*. Academic Press.
- JENSEN, H. W., MARSCHNER, S. R., LEVOY, M., AND HANRAHAN, P. 2001. A practical model for subsurface light transport. In *Proc. ACM SIGGRAPH*, 511–518.
- LENSCH, H. P. A., GOESELE, M., BEKAERT, P., MAGNOR, J. K. M. A., LANG, J., AND SEIDEL, H.-P. 2003. Interactive rendering of translucent objects. *Computer Graphics Forum* 22, 2, 195–205.
- MATUSIK, W., AJDIN, B., GU, J., LAWRENCE, J., LENSCH, H. P. A., PELLACINI, F., AND RUSINKIEWICZ, S. 2009. Printing spatially-varying reflectance. *ACM Trans. Graph.* 28, 3, 1–6.

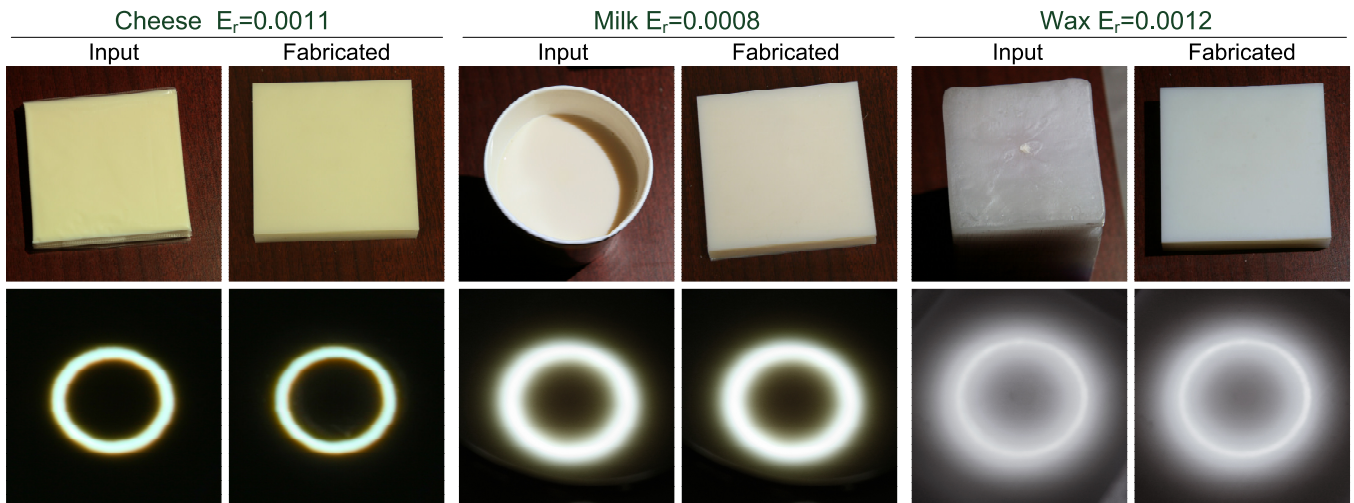


Figure 7: Comparison of scattering effects of real material samples and fabricated volumes under circular lighting.

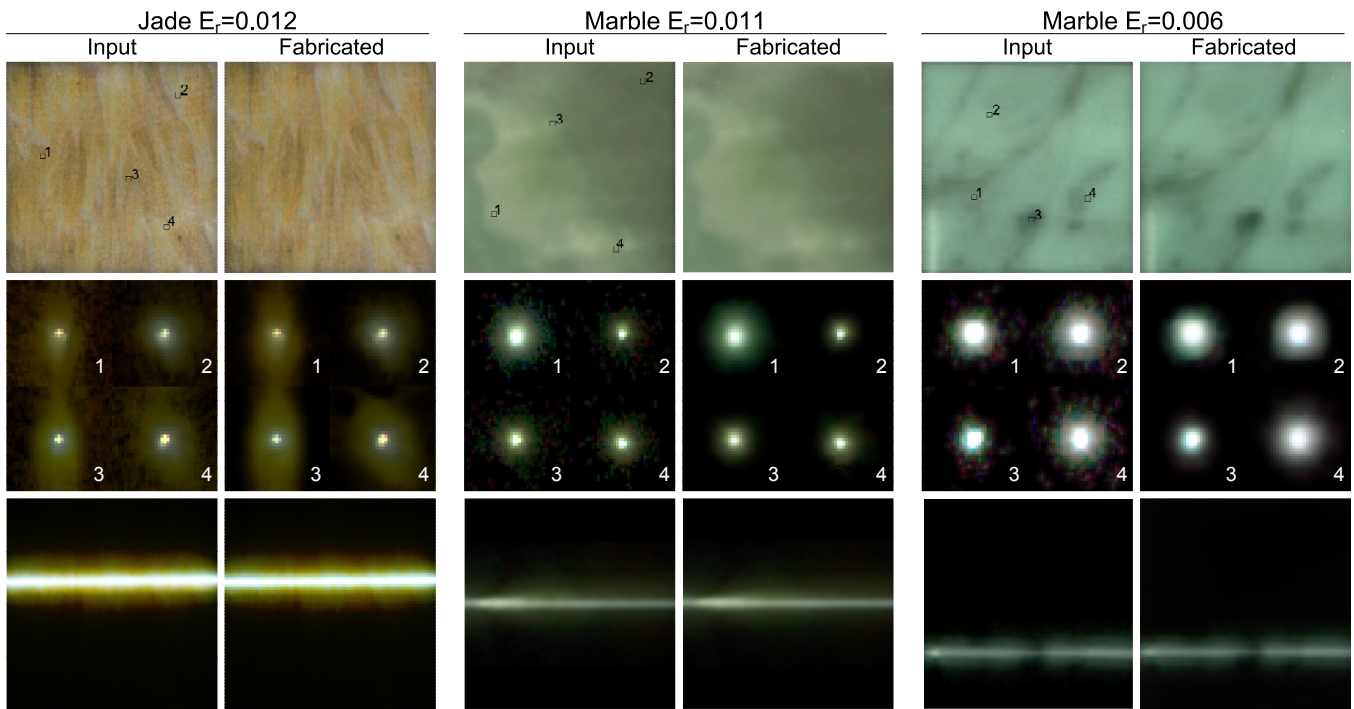


Figure 8: Comparison of the rendering results of input heterogeneous BSSRDFs and the photographs of fabricated volumes under different lightings.

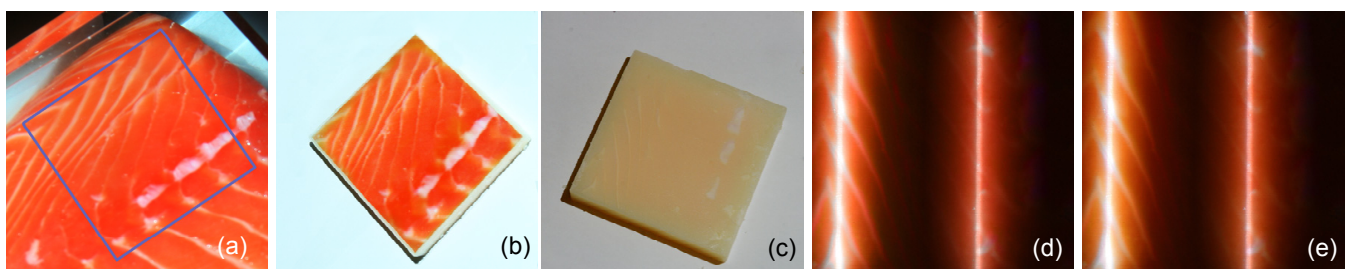


Figure 9: Fabricated salmon with BSSRDF measured from a real salmon slice. (a) Photograph of real salmon slice under diffuse lighting. The BSSRDF measured in the blue box is used as input to our system. (b) Photograph of result volume under diffuse lighting. (c) Rendering results of the input BSSRDF under line lighting. (d) Photograph of result volume taken under the same line lighting. (e) Another photograph of the fabricated salmon volume under line lighting.

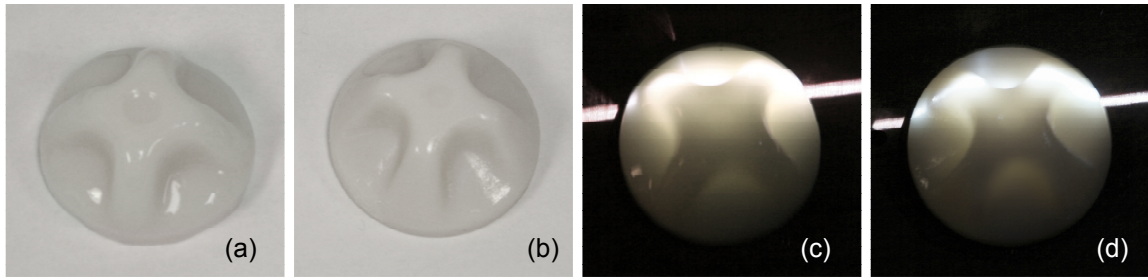


Figure 10: Fabricated jello. (a) A real piece of jello, the homogeneous BSSRDF of which is used as input to our system (b) A fabricated piece of jello generated by 3D printer. (c) Photograph of the real piece of jello under line lighting. (d) Photograph of the piece of fabricated jello under the same line lighting. The real jello and the fabricated one have the same size of 50mm × 50mm × 27mm

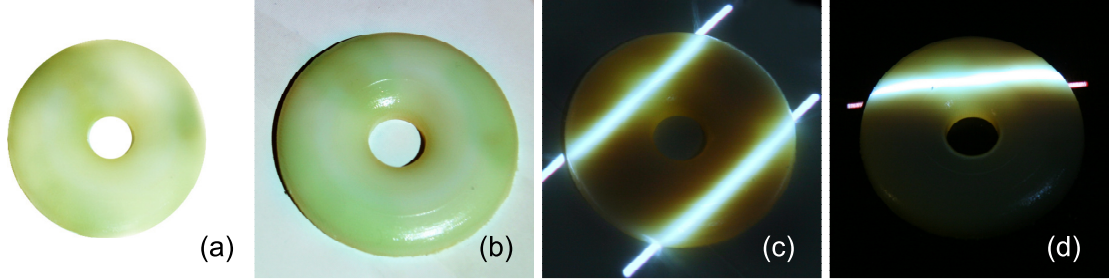


Figure 11: Fabricated round plate with designed jade-like subsurface scattering. (a) The input BSSRDF rendered with diffuse light. (b) Photograph of fabricated round plate under diffuse light. (c)(d) Appearances of the fabricated round plate captured under different lightings. The object size is 82mm × 82mm × 9mm

MOUNT, D., AND ARYA, S. 1997. ANN: A library for approximate nearest neighbor searching. In *CGC 2nd Annual Fall Workshop on Computational Geometry*.

NICODEMUS, F. E., RICHMOND, J. C., HSIA, J. J., GINSBERG, I. W., AND LIMPERIS, T. 1977. *Geometrical Considerations and Nomenclature for Reflectance*. National Bureau of Standards (US).

PEERS, P., VOM BERGE, K., MATUSIK, W., RAMAMOORTHI, R., LAWRENCE, J., RUSINKIEWICZ, S., AND DUTRÉ, P. 2006. A compact factored representation of heterogeneous subsurface scattering. *ACM Trans. Graph.* 25, 3, 746–753.

PHARR, M., AND HANRAHAN, P. M. 2000. Monte Carlo evaluation of non-linear scattering equations for subsurface reflection. In *Proc. ACM SIGGRAPH*, 275–286.

PORUMBESCU, S. D., BUDGE, B., FENG, L., AND JOY, K. I. 2005. Shell maps. *ACM Trans. Graph.* 24, 3, 626–633.

PRESS, W. H., ET AL. 1992. *Numerical Recipes in C (Second Edition)*.

SONG, Y., TONG, X., PELLACINI, F., AND PEERS, P. 2009. SubEdit: a representation for editing measured heterogeneous subsurface scattering. *ACM Transactions on Graphics* 28, 3 (Aug.), 31:1–31:9.

STAM, J. 1995. Multiple scattering as a diffusion process. In *Euro. Rendering Workshop*, 41–50.

TARIQ, S., GARDNER, A., LLAMAS, I., JONES, A., DEBEVEC, P., AND TURK, G. 2006. Efficiently estimation of spatially varying subsurface scattering parameters. In *11th Int'l Fall Workshop on Vision, Modeling, and Visualization 2006*, 165–174.

TONG, X., WANG, J., LIN, S., GUO, B., AND SHUM, H.-Y. 2005. Modeling and rendering of quasi-homogeneous materials. *ACM Trans. Graph.* 24, 3, 1054–1061.

VILBRANDT, T., MALONE, E., H., L., AND PASKO, A. 2008. Universal desktop fabrication. In *Heterogeneous Objects Modelling and Applications*, 259–284.

WANG, R., TRAN, J., AND LUEBKE, D. 2005. All-frequency interactive relighting of translucent objects with single and multiple scattering. *ACM Trans. Graph.* 24, 3, 1202–1207.

WANG, J., ZHAO, S., TONG, X., LIN, S., LIN, Z., DONG, Y., GUO, B., AND SHUM, H.-Y. 2008. Modeling and rendering of heterogeneous translucent materials using the diffusion equation. *ACM Trans. Graph.* 27, 1, 9:1–9:18.

WANG, R., CHESLACK-POSTAVA, E., LUEBKE, D., CHEN, Q., HUA, W., PENG, Q., AND BAO, H. 2008. Real-time editing and relighting of homogeneous translucent materials. *The Visual Computer* 24, 565–575(11).

WEYRICH, T., MATUSIK, W., PFISTER, H., BICKEL, B., DONNER, C., TU, C., MCANDLESS, J., LEE, J., NGAN, A., JENSEN, H. W., AND GROSS, M. 2006. Analysis of human faces using a measurement-based skin reflectance model. *ACM Trans. Graph.* 25, 3, 1013–1024.

WEYRICH, T., PEERS, P., MATUSIK, W., AND RUSINKIEWICZ, S. 2009. Fabricating microgeometry for custom surface reflectance. *ACM Trans. Graph.* 28, 3, 1–6.

XU, K., GAO, Y., LI, Y., JU, T., AND HU, S.-M. 2007. Real-time homogenous translucent material editing. *Computer Graphics Forum* 26, 3, 545–552.

Appendix: We compute the gradient of objective function relative to material properties in a voxel \mathbf{v} with the adjoint method [Wang et al. 2008a]:

$$dE_h/d\kappa(\mathbf{v}) = \sum_{i=1}^{N_f} \nabla \varphi_i(\mathbf{v}) \cdot \nabla \varphi_i(\mathbf{v}) - 2\lambda \Delta \kappa(\mathbf{v}), \quad (13)$$

$$dE_h/d\sigma_a(\mathbf{v}) = \sum_{i=1}^{N_f} \varphi_i(\mathbf{v}) \varphi_i(\mathbf{v}), \quad (14)$$

where $N_f = N_x \times N_y$ and $\varphi_i(\mathbf{v})$ is determined by the original diffusion equation with the unit illumination at each surface point \mathbf{x}_i , and $\varphi(\mathbf{v})$ is determined by the adjoint equation of the original diffusion equation:

$$\nabla \cdot (\kappa(\mathbf{v}) \nabla \varphi(\mathbf{v})) - \sigma_a(\mathbf{v}) \varphi(\mathbf{v}) = 0, \quad \mathbf{v} \in V, \quad (15)$$

$$\varphi(\mathbf{x}) + 2c\varphi(\mathbf{x}) \frac{\partial \varphi(\mathbf{x})}{\partial \mathbf{n}} = \frac{2c}{\pi} (R_d(\mathbf{x}_i, \mathbf{x}) - R'_d(\mathbf{x}_i, \mathbf{x})), \quad \mathbf{x} \in A, \quad (16)$$

where $R_d(\mathbf{x}_i, \mathbf{x}) - R'_d(\mathbf{x}_i, \mathbf{x})$ is the difference between the measured BSSRDF $R_d(\mathbf{x}_i, \mathbf{x})$ and BSSRDF $R'_d(\mathbf{x}_i, \mathbf{x})$ computed from the original diffusion equation with the unit illumination at \mathbf{x}_i .